Charge pattern detection through electrostatic array sensing

Zaihao Tian [a], Ping Lu [a,b], Jo Grundy [a], Terence Harvey [a], Honor Powrie [a,c], Robert Wood [a,*]

[a] National Centre for Advanced Tribology, University of Southampton, Southampton SO17 1BJ, United Kingdom
[b] Centre for Manufacturing and Materials, Coventry University, Coventry CV1 5FB, United Kingdom
[c] GE Aerospace, Eastleigh SO53 4YG, United Kingdom

ARTICLE INFO

ABSTRACT

As reported in previous work, electrostatic charge induced by contact potential difference (CPD) arising from oxidational wear can be detected by electrostatic button sensors. However, to detect signs of localised wear and to investigate the mechanisms involved, the charge distribution on worn regions needs to be measured. Therefore, this paper investigates the evolution of surface charge during wear processes, its interplay with friction, and the correlation between charge distribution and surface chemistry. An electrostatic bar sensor and an array sensor were initially calibrated using CPD patterns generated by dissimilar metal inserts in steel plates. After appropriate signal processing, the sensor outputs exhibited excellent agreement with the electric field strength modelled using COMSOL Multiphysics. Subsequently, the bar sensor was integrated into a reciprocating tribometer for in-situ detection of oxidational wear of steel-on-steel rubbing contacts, followed by ex-situ array sensing of worn regions. Positive picocoulomb-level surface charge during the evolution of oxidational wear were successfully detected by the bar sensor and were found to correlate to changes in friction coefficient. The array sensor effectively mapped the distribution of surface charge. EDS mapping suggested patchy formation of Fe_3O_4 layers over the worn areas, and these patches correlated to the surface charge map. Increased electrostatic charge levels were associated with higher concentrations of oxidational wear. Therefore, this paper evaluates the potential of electrostatic array sensors to spatially resolve surface charge patterns induced by surface chemistry transformations, which enables the monitoring of localised and smaller-scaled machinery component deterioration and provides additional information for machinery diagnosis.

1. Introduction

Over the past three decades, electrostatic sensing technology has been developed and applied in various fields, including the flow measurement of pneumatically conveyed solids, measurement of particulate emissions, monitoring of fluidised beds, on-line particle sizing, burner flame monitoring, speed and radial vibration measurement of mechanical systems, and condition monitoring of power transmission belts, mechanical wear, and human activities [1]. When used as a condition monitoring method, this technique has advantages in sensitivity and can directly measure the problem source rather than a secondary effect, such as vibration, which is important for the early detection of machinery component deterioration. In addition, charge sensing also enjoys the advantages of simplicity of construction, cost-effectiveness and suitability for a wide range of installation conditions [1].

Wear mechanisms within tribological contacts could potentially generate charge [2,3], as illustrated in Fig. 1. The current work focuses on surface charges induced by the contact potential difference (CPD). CPD is an electrostatic potential that exists between samples of two dissimilar electrically conductive materials (metals or semiconductors with different work functions) that have been brought into thermal equilibrium with each other, usually through a physical contact.

The CPD caused by different metals can be explained by work function theory as depicted in Fig. 2. The work function is defined as the minimum amount of energy required, in a vacuum, to extract an electron from the Fermi level of a conducting phase through a surface. Different materials have different Fermi levels, resulting in different work functions. When two metals, M_a and M_b, come into contact, their Fermi energies (ϕM_a and ϕM_b) equalise, generating an electrical charge on the respective surfaces. This charge separation results in a CPD, V_{CPD}, between the two surfaces, which is related to the difference in their work functions, as represented in Eq. 1 [4].

$$eV_{CPD} = \phi M_a - \phi M_b \qquad (1)$$

---

* Corresponding author.
  E-mail address: r.wood@soton.ac.uk (R. Wood).

CPD can also be generated by an imbalance of charge on the surface of worn materials, or the formation of tribologically generated phase transformations or oxide layers [4–11]. Oxidational wear is a mild wear mechanism where thick and brittle oxide films are formed in the contact areas due to frictional heating between the contacting surface asperities. These oxide layers usually appear as patches on the sliding surfaces. When the oxide reaches a critical thickness, usually 1–3 μm, the oxide breaks up and eventually appear as wear debris [12,13]. When a region on the metal surface undergoes oxidation or accumulates oxide wear debris, there is typically an increase in the work function [14]. However, the charge on the nascent surface relaxes rapidly. As a result, these newly oxidised regions exhibit a higher work function than the surrounding areas. This difference in work function leads to the development of charge differences and the consequent generation of a CPD [11]. The positively charged oxidised regions could be potentially detected by electrostatic sensors. Although the localised static charge is fixed at the component surface, it appears as a dynamic effect when detected from an electrostatic sensor if the surface moves relative to the sensor. This effect appears as an electrostatic charge peak relative to the background charge level [15].

Booth [10] investigated the electrostatic response to CPD caused by wear in engine components in a motored TU3 cam-follower test. The test was conducted under oil starvation, and an electrostatic button sensor was utilised to monitor the charge on the cam surface. The root mean square (RMS) charge initially started at a low level and gradually increased as wear progressed. The charge map and surface observations indicated that the development of the high charge region corresponded to the occurrence of adhesive wear. Additionally, oscillations were observed in the charge data, which were believed to be linked to activities such as oxidation, delamination, and re-oxidation. In a study conducted by Morris [11], experimental investigations were carried out to monitor the oxidational wear performance of bearing steel under unlubricated sliding conditions using an electrostatic button sensor. The primary wear mechanism observed was mild oxidational wear, which produced a significant response from the electrostatic sensor at high wear rates. The dominant charging mechanism was believed to be related to the CPD between nascent and oxidised regions. The oxidised regions had a higher work function than nascent metal surfaces,

resulting in a positive charge accumulation. The correlation between the electrostatic sensor signal and the formation and delamination of oxide films indicated that electrostatic charge monitoring was an effective technique for determining the dynamic conditions of dry sliding steel contacts.

Although various surface failure modes have been detected by the electrostatic sensing technique, most of the studies focused on the gross measurement over width greater than 10 mm [4–10] rather than higher spatial resolutions for pattern detection. As a result, the important information of the failure severity in local regions may be overlooked. Taking inspiration from the design of fingerprint array sensors, a new design of an electrostatic array sensor has been proposed. The fingerprint array sensor is a type of capacitive sensor that employs an array of tiny sensing elements to capture the fingerprint image [16]. It consists of numerous small capacitors, each capable of measuring the electrical capacitance between the sensor surface and the ridges and valleys of the fingerprint. When a finger is placed on the sensor surface, the capacitance at each sensing element varies according to the topography of the fingerprint, creating a unique electrical pattern. The advantages of the fingerprint array sensors over traditional sensors include higher resolution, improved image quality, and enhanced spoof detection capabilities. The higher resolution allows for more detailed and accurate fingerprint images, resulting in more reliable identification and verification. To detect the charge pattern associated with CPD at a higher resolution and obtain information about localised wear phenomenon, an electrostatic array sensor was developed and tested.

Electrostatic array sensors have been employed for the assessment of particle velocity and concentration within gas-solid systems and to improve temporal resolution. The generation of electrostatic charge on particles arises from frictional contact and collisions between particles and pipe walls [17,18]. In instances of faults occurring within the gas path components of gas turbines, charged debris is produced and released into the exhaust gas. Using a circular array of electrostatic sensors, the amount and charge of debris were identified [19,20]. Such data serve as important indicators of the fault severity. Yong Yan and colleagues [21–24] measured the velocity and concentration of pneumatically conveyed particles using electrostatic array sensors. The magnitude of the electrostatic charge increases with the increase in the
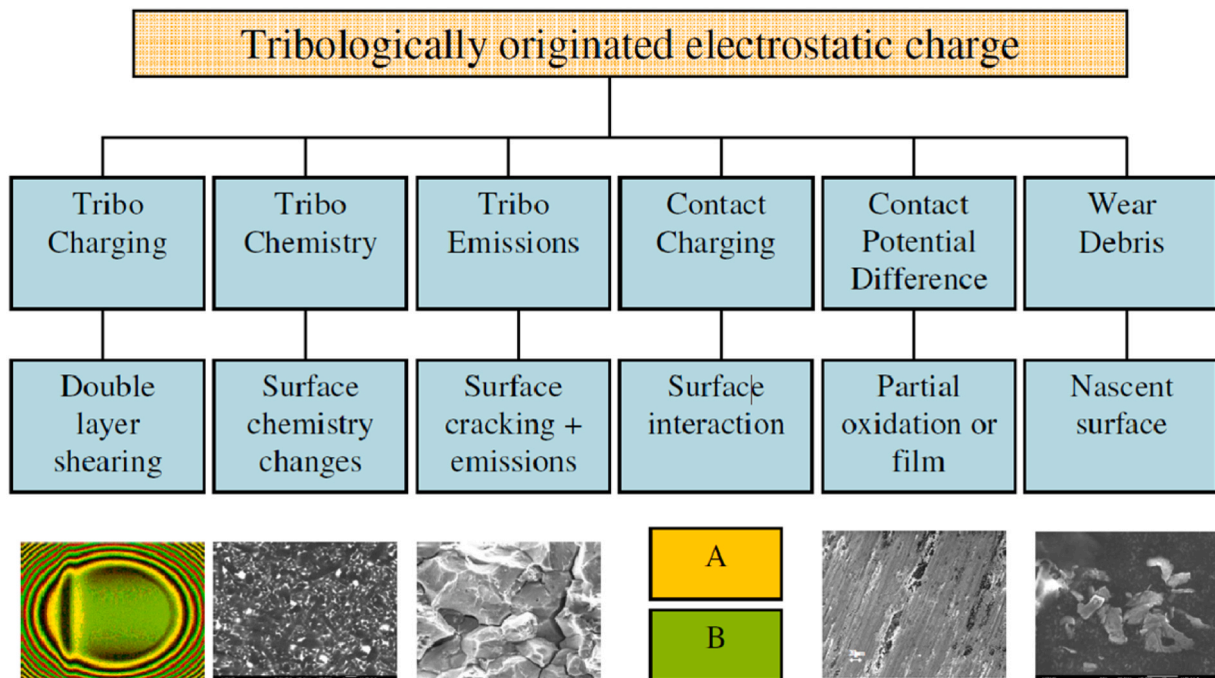

Fig. 1. Scheme of charge generated from various tribological mechanisms [32].

particle concentration. The particle velocity was determined by spatial filtering and cross-correlation method. Their experimental setups encompassed various configurations: an array of five sensors spanning the diameter of the pipe [21,22], an array of 2 × 3 pairs of electrostatic sensors [23], and a linear array of electrostatic sensors [24]. A linear array of arc-shaped electrostatic sensors has also been used to monitor the velocity of particles in gas-solid fluidised beds [25,26]. Reference [24] suggests that in order to optimise the design of electrostatic array sensors, careful consideration should be given to parameters such as electrode number, width, and spacing. These parameters are noted to influence signal quality significantly.

The work in this paper presents a new array sensor design and detection of charge pattern associated with CPD and oxidational wear from dry sliding tests. Compared with previous electrostatic button sensors used for gross measurement, the proposed array sensor demonstrates higher spatial sensitivity. Using several smaller sensing faces facilitates the detection of localised wear phenomenon, enabling the generation of a charge map to identify wear distribution and mechanisms. Additionally, through signal averaging across sensing elements, the sensor efficiently mitigates random noise and enhances the signal-to-noise ratio. This enables earlier detection of surface degradation to facilitate improved maintenance schedules and associated benefits of these.

2. Materials and method

2.1. Principles of electrostatic charge detection and sensor design

The electrostatic sensing system comprises a passive sensor and a charge amplifier, as illustrated in Fig. 3. The sensor consists of a sensing element, an insulator, and a grounded shield. It operates based on the principle of electrostatic charge induction. Electrostatic induction is a phenomenon where the electric charge in an object is redistributed due to the influence of nearby charges. When a charged object moves in front of the sensor face, some of the electric field lines resulting from the charge terminate on the sensor face. This results in the redistribution of electrons in the sensor face, generating a charge flow to balance the additional charge in the vicinity of the sensor [15]. If the object is positively charged, the free electrons on the electrode will be drawn towards the charged object and therefore the charge flow will be positive. By measuring the charge flow, it is possible to monitor the polarity and magnitude of the charge. The low-level charge, which is typically less than 1 picocoulomb, is measured by a charge amplifier which converts the charge into a voltage signal and then amplifies it, thus making it suitable for subsequent data manipulation.

As a result of the finite area of the sensor, not all the electric field lines will terminate on the sensor face, leading to an incomplete detection of the charge Q. The quantity of charge detected by the sensor, denoted as Q_A, depends on several factors and may be estimated using the following equation:

$$Q_A \sim \frac{Q * A}{x^2} \tag{2}$$

Where A is the sensor area and x is the clearance between the charged

particle and the sensor face. Eq. (2) shows that sensor sensitivity to a charge source relies on several critical factors [15]. The sensitivity is amplified by an increase in charge magnitude, as a stronger charge generates a more intense electric field that induces a more pronounced charge on the sensor face. A larger sensing face area offers a broader surface for electric field interaction, leading to an enhancement in the induced charge. Conversely, the induced charge diminishes as the separation distance between the charge and the sensor increases since the electric field strength decreases with distance. Furthermore, the speed at which a charged object moves under the sensing face can impact the induced charge, as faster motion induces a more rapid change in the electric field, consequently leading to a stronger induced charge due to electromagnetic induction.

Based on the principle of electrostatic charge detection, two sensors were designed and employed in this project: a bar sensor for gross charge measurement and an array sensor for charge pattern detection. The structure of the bar sensor is depicted in Fig. 4. In Fig. 4(a), the sensor's sensing element presents a 'T' shape with a width of 20 mm and an effective sensing area of 46 mm^2. This element is made of copper, and it is electrically isolated from its aluminium shell by an insulator as depicted in Fig. 4(b). The aluminium shell acts as an earth shield, providing protection by shielding the sensing element from external electrical interference and charges from the surrounding environment. This shielding action helps maintain the sensor's performance and accuracy by safeguarding it against unwanted external influences.

To transform the detected charge into voltage signals, the sensor interfaces with a Brüel & Kjær 2635 charge amplifier with an amplification factor of 1 V/pC. Subsequently, the charge amplifier is linked to a Data Translation DT9801 data acquisition card which transforms the voltage signal to digital signal for further processing.

The three-channel array sensor comprises of three sensing elements, an insulator and an earth shield, as depicted in Fig. 5. As shown in Fig. 5 (a), the three sensing elements are denoted as Ch1 (Channel 1 etc.), Ch2, and Ch3, respectively. They are flat copper plates with a width of 4 mm and a height of 1.5 mm, which determines the effective sensing area of 6 mm^2. The copper plates were fabricated by etching onto a non-conductive insulator, and the insulator was assembled into an earth shield as shown in Fig. 5(b). The innovative design of the array sensor was driven by the necessity for higher resolution, improved charge pattern detection, and noise reduction through cross-comparison measurement. The area of sensing element determines the resolution of the sensor, i.e., the smaller the area of sensing element, the higher the resolution [5]. In contrast to the bar sensor, which is 20 mm wide, the array sensor has a 4 mm width, ensuring an enhancement in resolution. This heightened resolution allows the sensor to detect localised surface charges, a capability often overlooked in gross measurements, thereby enabling the detection of intricate charge patterns and thus localised surface wear phenomena. Furthermore, the reliability of the sensor is ensured by having three sensing elements. By averaging signals from the three sensing elements while scanning the same area, the sensor effectively eliminates random noise and highlights signals correlated to the features of interest on surface. Each sensing element is connected to a BNC cable through soldering at their back surfaces.

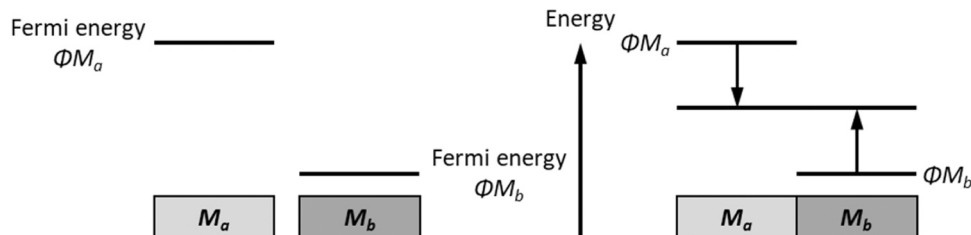The sensor is connected to a Kistler LabAmp 5165 A charge amplifier

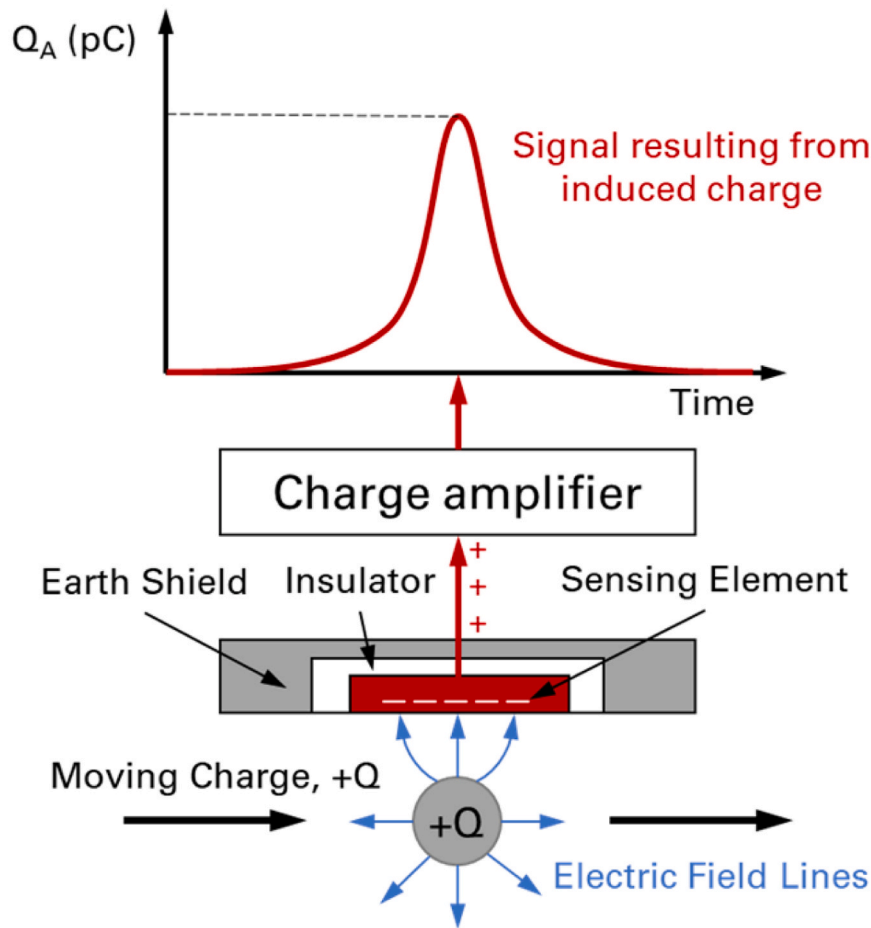**Fig. 2.** An illustration of contact potential difference (CPD) theory [11].

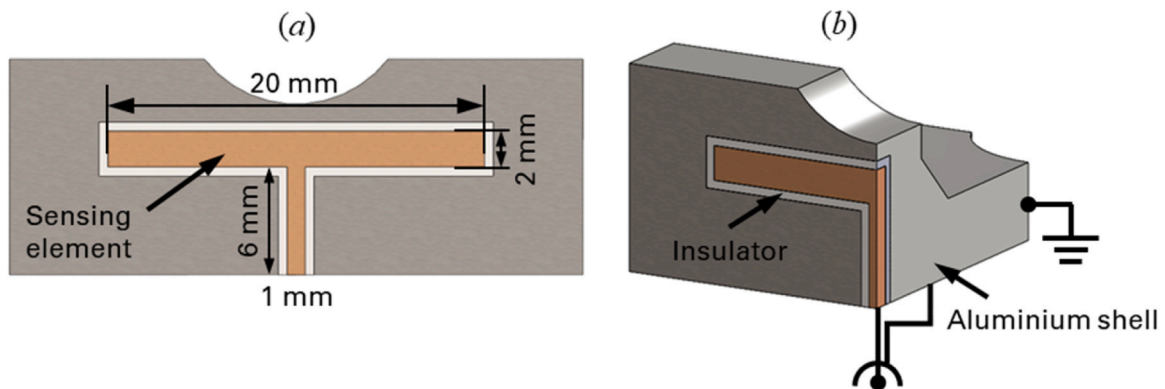**Fig. 3.** Schematic of the inductive electrostatic sensing system [11].

Fig. 4. (a) Surface view of the bar sensor (b)Cross-section view of the bar sensor.

with an amplification ratio of 1 V/pC. Furthermore, the charge amplifier is interfaced with an NI DAQ USB 6002 data acquisition card. This device allows for signal acquisition at a maximum sampling rate of 50 kHz with a resolution of 16 bits.

2.2. Charge sources and sample design

To generate a CPD of known polarity (i.e., positive or negative) for calibration tests, a matrix of 2 mm diameter holes was drilled into BO1 BS4659 tool steel plates, allowing for various metals to be inserted. In the subsequent wear tests, the inhomogeneity of wear mechanisms and their evolution within the contact area led to the formation of localised

regions of active wear within the wear scar area of 20 mm × 25 mm. Therefore, a diameter of 2 mm was selected to match the anticipated scale of such localised wear activity and the CPD it would produce. The arrangement of the inserts is illustrated in Fig. 6. The steel plates contain four rows of inserts, denoted as R1 (Row1 etc.), R2, R3 and R4, with a spacing of 5 mm between the centre of the inserts on adjacent rows. The dimensions of the sensing elements of the array sensor were determined with consideration of the arrangement of the inserts. The width of the electrodes was configured to sufficiently encompass one to two inserts. The height of the electrodes was set to be smaller than the distance between adjacent rows of inserts to prevent signal overlap. Three plates were fitted with inserts of steel, aluminium and solder respectively for
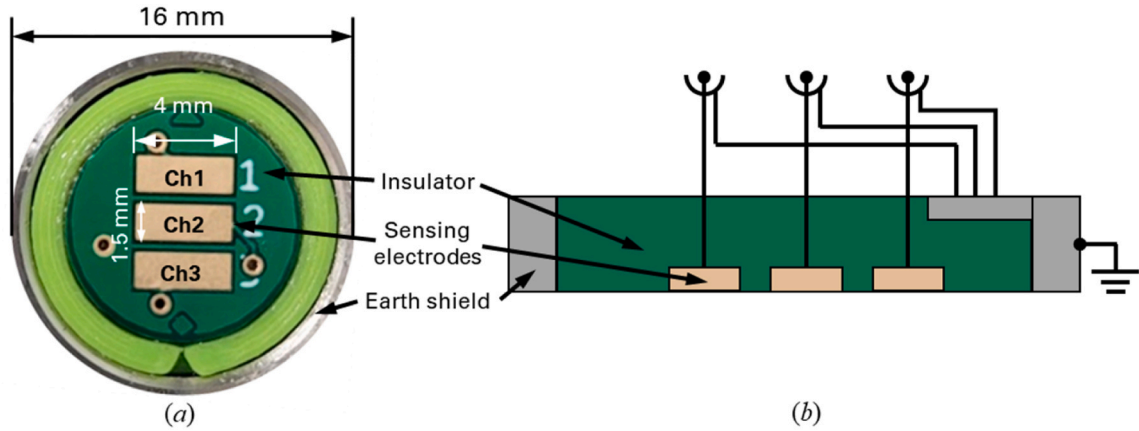
Fig. 5. (a) Surface view of the array sensor (b)Cross-section view of the array sensor.
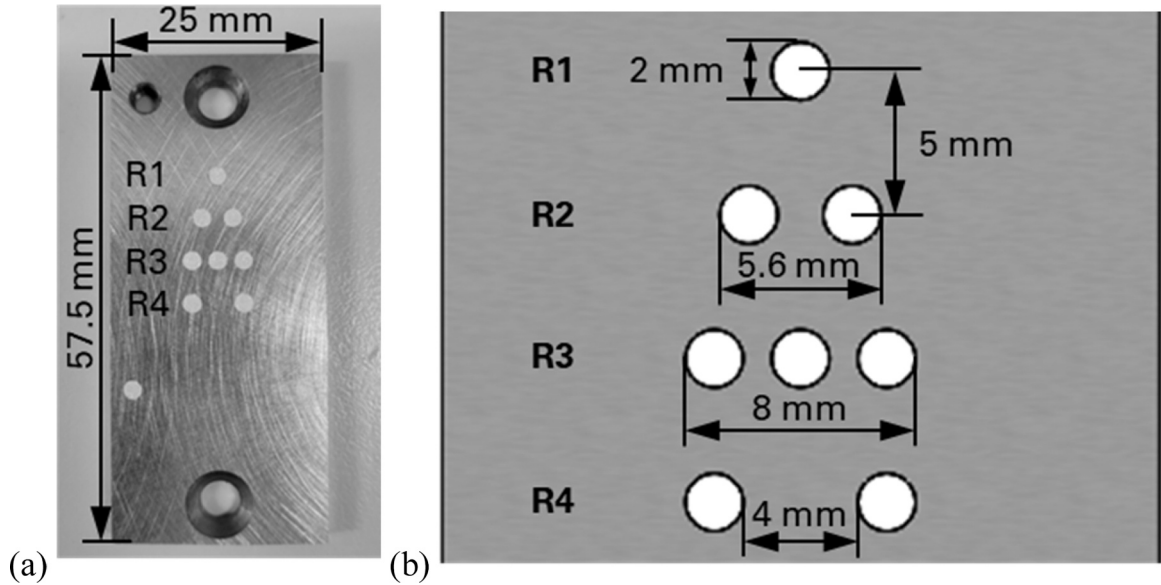

Fig. 6. (a) Image of a calibration sample (b) Size and arrangement of inserts.

calibration tests. When using an electrostatic sensor to scan a plate, the source of the charge comes from the potential difference between the inserts and the plates. In response, electrons within the sensor rearrange to neutralise the additional charge in the vicinity of the sensor, resulting in a current flow. This flow of current is subsequently measured by the conditioner.

The composition of the steel, aluminium, and solder inserts was determined by energy-dispersive X-ray spectroscopy (EDS) analysis. The compositions and literature values for the work functions of these three metals [27] are shown in Table 1. The solder inserts comprised a mixture of tin and lead. Based on the proportions and the work functions of lead and tin, the work function of the solder is estimated to be 4.32 eV. Prior to testing, the plates were ground to ensure their flatness with a surface roughness (Rq) of 0.2 μm. Subsequently, the plates were subjected to

ultrasonic cleaning using acetone to eliminate any contaminants present on the surface.

The samples used in the subsequent wear tests were roller made of AISI 52100 steel and plate made of BO1 BS4659 tool steel. The properties of the two steels are listed in Table 2. The roller had a diameter of 6 mm and a length of 20 mm, while the plate was 60 mm in length, 25 mm in width, and 4 mm in thickness.

2.3. Test matrix and test machines

To validate the feasibility of using both sensors in charge detection, a series of calibration tests were conducted. The calibration of the bar sensor was carried out on a TE77 reciprocating tribometer using a steel

Table 1
Compositions and work functions of different metals [27].

	Fe	Al	Pb	Sn
Steel composition (wt%)	94.0			
Al composition (wt%)	4.4	93.1		
Solder composition (wt%)	0.45		49.57	49.98
Work function (eV)	4.60	4.28	4.25	4.42

Table 2
Properties of materials of roller and plate.

Grade	Density (kg/m³)	Elastic modulus (GPa)	Poisson ratio	Hardness (HV)
Roller material: AISI 52100	7810	200	0.28	848
Plate material: BO1 BS4659 tool steel	8000	230	0.29	800

plate with aluminium inserts. Meanwhile, the array sensor's calibration was performed using three plates inserted with aluminium, solder, and steel, and the calibration was conducted on a 3D scanner. To create oxidational wear, a roller-plate contact setup was employed on the TE77 reciprocating tribometer. Throughout the tests, the bar sensor was employed to continuously monitor the evolution of surface charge in real-time. Subsequently, following the completion of the tests, the array sensor was engaged to scan the wear scar and generate charge maps. A summary of the calibration tests and wear tests is presented in Table 3. The tests were conducted under controlled room temperature (23 ℃) and a relative humidity level of 70%.

2.3.1. Sensor calibration setups

To assess the ability of the electrostatic system to detect CPD, scans of the metal inserts matrix were conducted using both the bar sensor and the array sensor. Calibration of the bar sensor was performed using a TE77 high-frequency friction machine, manufactured by Phoenix Tribology Ltd. Newbury, UK, with the setup configuration depicted in Fig. 7(a). The test plate was securely fixed on a stable platform, and the bar sensor was mounted on a reciprocating carrier, with its sensing element positioned at a distance of 0.4–0.45 mm from the plate surface. The clearance was adjusted using a feeler gauge. The reciprocating motion was driven by a mechanical assembly comprising a motor-driven cam and scotch yoke mechanism. The scanning length and the reciprocating frequency were set at 15 mm and 1 Hz, respectively. The scanning path of the sensor over the insert matrix is shown in Fig. 7(b).

For calibration of the array sensor, a modified 3D scanner adapted from an Ender-3 Pro 3D printer was employed, as demonstrated in Fig. 8 (a). The calibration plate was securely affixed onto a flat printer table which was capable of horizontal movement along the y-axis. The sensor, positioned above the plate, was able to move in both the x and z directions. Precision in movement was achieved through the use of stepper motors, offering control over movements with a precision of 0.1 mm in x and y directions. The scanning path over the insert pattern is presented in Fig. 8(b) with a length of 15 mm. Care was taken to ensure the alignment of the direction of the sensing elements corresponded to the scanning direction to obtain consistent signals and to allow effective signal averaging. Tests were conducted at four different clearances between the plate and sensor face: 0.2 mm, 0.4 mm, 0.6 mm, and 0.8 mm. The data acquisition sampling rate was set at 1000 Hz.

2.3.2. Tribological feasibility testing setups

A TE77 high frequency friction machine was employed to conduct wear tests to investigate the charge generation during the surface wear process. A schematic diagram of the roller-plate friction pair used in the wear tests is shown in Fig. 9. The carrier housing a roller had a reciprocal motion against a stationary steel plate. The stroke length and the reciprocating frequency were set at 25 mm and 1 Hz, respectively. The roller was loaded against the steel plate using a lever mechanism. The

bar sensor was also mounted on the reciprocating carrier, with its sensing element positioned 0.4–0.45 mm away from the plate surface. The clearance was set using a feeler gauge. The frictional interaction between the roller and the plate was monitored using a piezoelectric transducer. The sampling rate of the piezoelectric transducer and the electrostatic bar sensor was 1000 Hz.

Two consecutive experiments were performed on a roller-plate pair with the objective of inducing oxidational wear through dry sliding contact. The test conditions are provided in Table 4, and are based on experimental conditions detailed in a previous study [11], where oxidational wear was successfully generated in unlubricated steel contacts.

2.4. Comparison of sensor calibration test data with COMSOL simulation

2.4.1. Test data processing

To enhance the electrostatic signal of the charge patterns and to eliminate random noise, the time-domain analysis technique of signal averaging was employed due to the periodic nature of the electrostatic sensor signal. The electrostatic signals from both the reciprocating TE77 and 3D scanner underwent averaging. Sampling was synchronised with the reciprocating motion, with one signal average produced after five strokes. This approach enhanced synchronous signals while suppressing random and unrelated effects, enabling clear identification of consistent signals generated by the inserts. The signal averaging concept is illustrated in Fig. 10, where each signal average is represented as a line plot along the x-axis, representing the start and end of the stroke, while the y-axis represents the magnitude of the electrostatic charge. The presence of high-frequency noise was attributed to electromagnetic interference (EMI) originating from the motor and power supply of the TE77 machine and 3D scanner, as well as mild vibrations occurred during scanner movement. The high-frequency nature of this noise, combined with the fact that only signals from 5 strokes were used for averaging, rendered signal averaging ineffective in the reduction of these noise. Therefore, after averaging, the data were further denoised using the Empirical Mode Decomposition (EMD) method to remove the high-frequency noise as illustrated in Fig. 9. The EMD approach employs an iterative screening process to decompose the original non-stationary signal into a sequence of new and improved signals, known as intrinsic mode functions (IMF), which represent the oscillatory components of the original signal [28]. In the specific example depicted in Fig. 9, the signal was decomposed into six IMFs. The first three of these IMFs corresponded to the noise signals, while the remaining three IMFs represented the charge signals. By summing up the latter three IMFs, the denoised charge signal were generated. These techniques were applied during calibration tests and oxidational wear tests.

2.4.2. Sensor response modelling

In order to investigate and understand the correlation between physical parameters such as sensor-sample clearance, charge pattern,

Table 3
Test matrix for calibration test and wear test.

| Test type	Sensor type	Test rig	Samples	Scanning length (mm)	Scanning speeds (mm/s)	Clearance
Calibration test	Bar sensor	TE77 reciprocating tribometer	Steel plate with Al inserts	15	50 mm/s	0.4 mm
	Array sensor	3D scanner	Steel plate with Al inserts, Steel plate with solder inserts, Steel plate with steel inserts	15	14.3 mm/s	0.2 mm, 0.4 mm, 0.6 mm, 0.8 mm
COMSOL modelling	Bar sensor		Steel plate with Al inserts (1pC assigned to each insert)	15	Parametric sweep with step size 0.2 mm	0.4 mm
	Array sensor		Steel plate with Al inserts (1pC assigned to each insert)	15	Parametric sweep with step size 0.2 mm	0.2 mm, 0.4 mm, 0.6 mm, 0.8 mm
Wear test	Bar sensor	TE77 reciprocating tribometer	Roller-plate	25	50 mm/s	0.4 mm
	Array sensor	3D scanner	Plates with wear scar	25	14.3 mm/s	0.4 mm
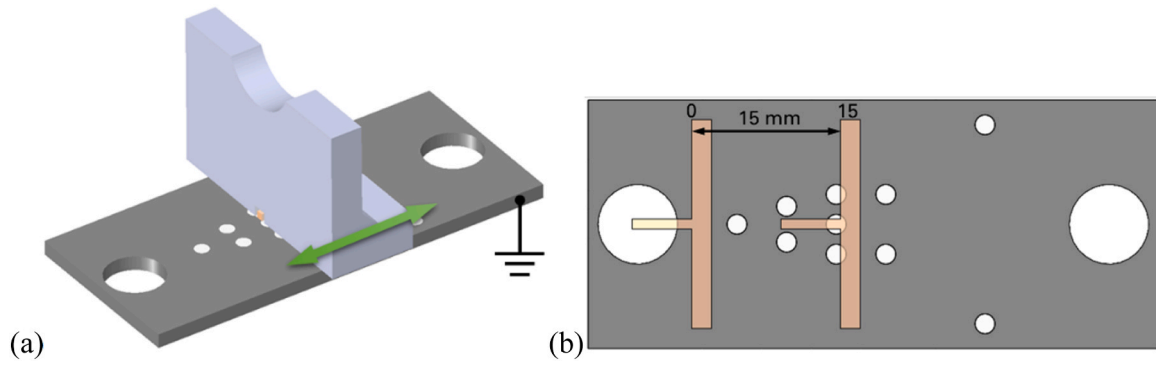
Fig. 7. (a) Configuration of bar sensor calibration and calibration sample (b) Scanning path over the insert matrix.
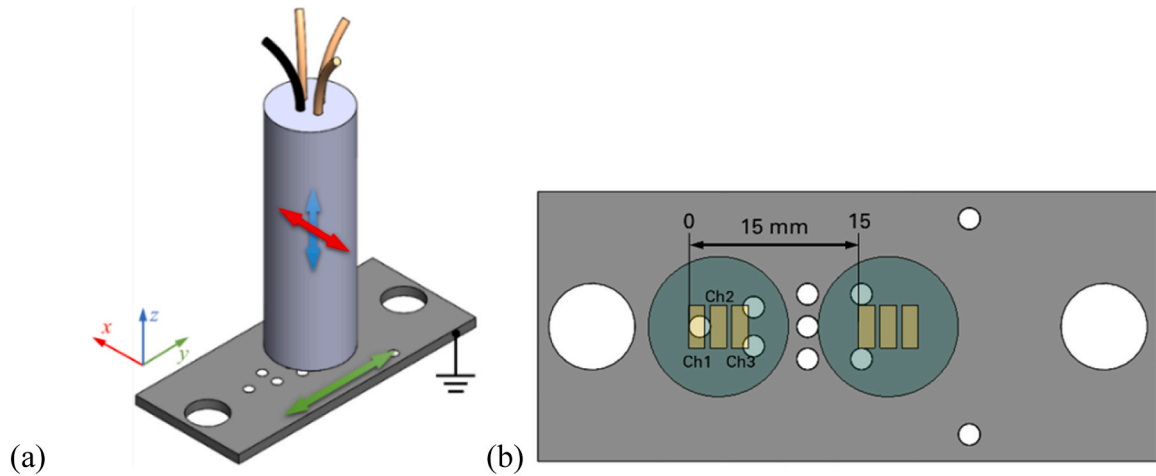

Fig. 8. (a) Configuration of array sensor calibration and calibration sample (b) Scanning path over the insert matrix.
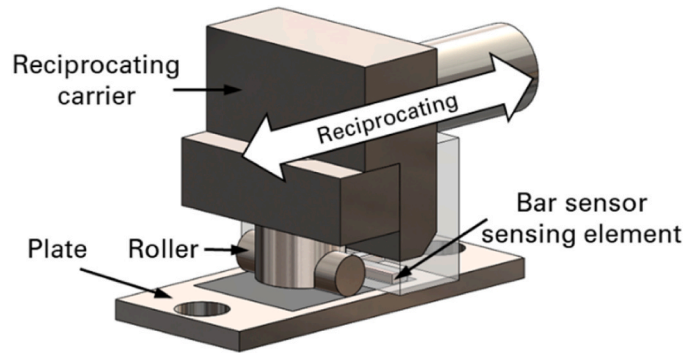

Fig. 9. Configuration of the roller-plate contact on TE77.

Table 4
Conditions for the wear tests.

No.	Load (kN)	Mean contact pressure (MPa)	Reciprocating frequency (Hz)	Stroke length (mm)	Duration (mins)
1	10	60	1	25	20
2	15	90	1	25	20

and induced charge, under various configurations and conditions, the Electrostatics, Boundary Elements (esbe) interface of COMSOL Multiphysics® was utilised to simulate electric fields resulting from static (non-moving) charges. This physics interface solves the Laplace equation for calculating the static electric field and, subsequently, the induced surface charge on each sensor element. The response of the sensor was simulated at different locations using a parametric sweep with an incremental step size of 0.2 mm. Fig. 11 illustrates the charge density model as predicted by COMSOL. In this test model, a 1pC charge was assigned to the surface of each aluminium insert. The selected charge value was based on one unit of charge, with metal permittivity derived from built-in COMSOL values. This approach was adopted to examine the correlation between clearance, charge pattern, and induced charge. To align the simulation outcomes with experimental findings, a scale factor was determined based on peak induced charges observed on sensors at a 0.4 mm clearance. This same scale factor was then utilised to validate results at other clearances (0.2, 0.6 and 0.8 mm).

2.5. Detection of charge induced in tribological feasibility testing

During the tribological feasibility tests, the bar sensor was used to monitor the real-time progression of the charge associated with wear, while the array sensor was used to generate ex-situ surface charge maps that reveal the distribution of oxidational wear.

2.5.1. Bar sensor for in-situ detection
Throughout the experimental testing, continuous monitoring of the surface charge on both the contact (i.e., worn) area and non-contact area of the material was achieved using a bar sensor. A schematic representation of the wear scar and the sensor scanned area can be found in Fig. 12.
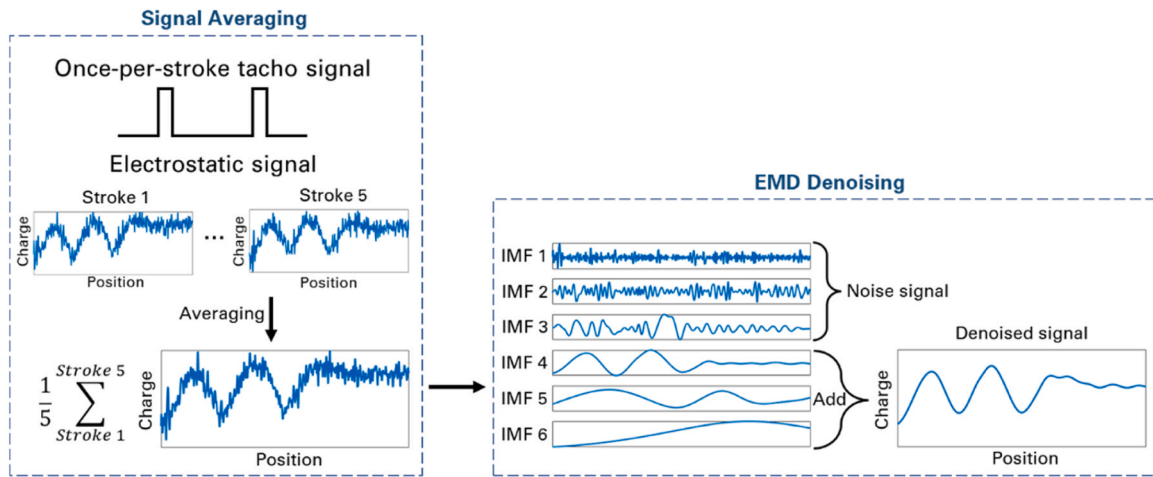
Fig. 10. Concept of signal processing: signal averaging and EMD denoising.
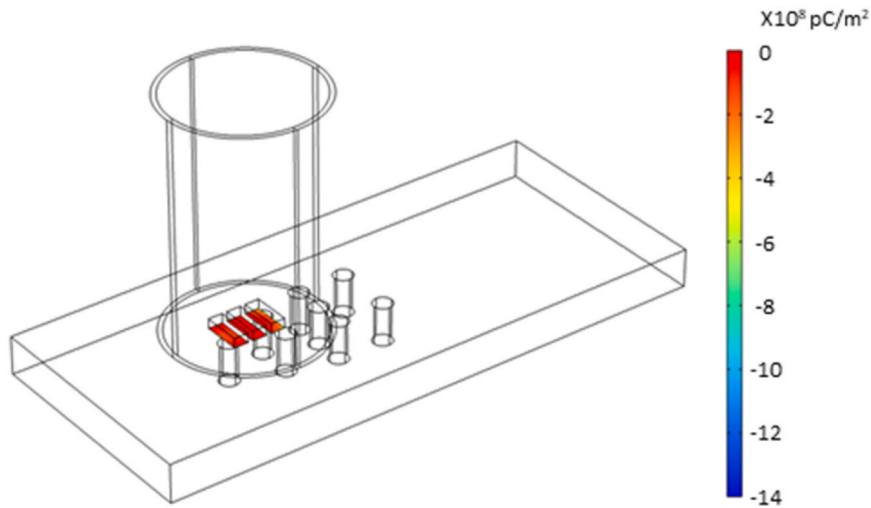

Fig. 11. Sensors and samples in COMSOL Multiphysics to study the induced charge on sensor elements.
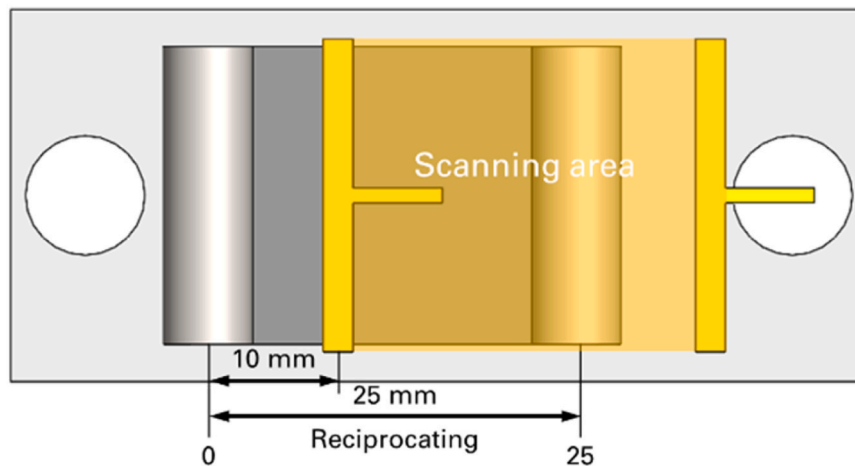

Fig. 12. Scanning area of bar sensor.

2.5.2. Array sensor for ex-situ mapping

Ex-situ surface charge maps were generated using the array sensor immediately after the completion of the two tests. The process of creating the charge maps is illustrated in Fig. 13. As shown in Fig. 13 (a), the scanning area consisted of five parallel scanning paths, all aligned with the reciprocating direction. Each path had a length of 20 mm, with a 4 mm separation between adjacent paths, which was equivalent to the width of the sensing element. The charge map was generated by using
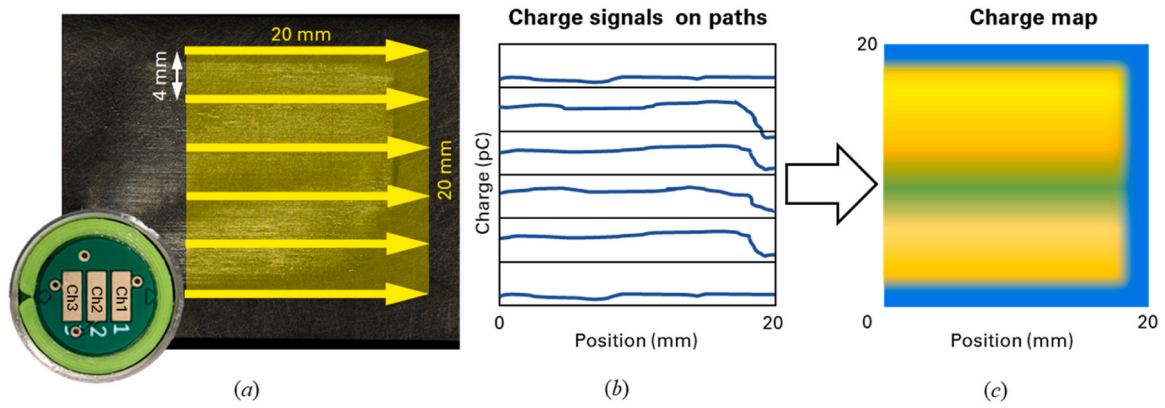
Fig. 13. (a) Scanning paths of array sensor and the scanning area (b) Illustration of charge signals on scanning paths (c) Charge map generated by interpolating signals on scanning paths.

the charge signals acquired from the five paths, as depicted in Fig. 13 (b). By using the interpolation function 'interp' in MATLAB, missing data between the five paths were filled in and the entire charge map was created. The resulting scanning area formed a square measuring 20 mm by 20 mm as shown in Fig. 13 (c). Blue denotes the region outside the wear track where surface charge is zero. Within the wear track, yellow and green represents positive charge, with yellow indicating a higher magnitude. It is worth noting that this scanning area matched the region scanned by the bar sensor during the test, thus facilitating a meaningful comparison between the results obtained from these two sensors.

## 3. Results and discussion

3.1. Calibration results

3.1.1. Bar sensor calibration results

A scale factor of 0.03 was applied to the simulated data for alignment with experimental findings. This factor was determined based on the peak induced charge on sensors when the sensor was positioned at 6 mm with a clearance of 0.4 mm. Fig. 14 (a) shows the comparison of the experimental and simulated bar sensor response to aluminium inserts. It is evident that the aluminium inserts produced negative signals, which can be attributed to the lower work function of aluminium relative to steel. Further insights are possible from the data in Fig. 14 (b), which show a gradient of approximately 0.9515 between the modelling results and the test data. Further, the coefficient of determination, or R-squared value, was calculated. The resultant value of 0.9396 suggests reasonable correlation between the model results and the experimental test results. However, at the start of the stroke position (0–4 mm), there is noticeable divergence between the modelling and test data which had the result of

lowering the R-squared value. This divergence was primarily due to the influence of the TE77 machine's motor as the sensor approaching the start of the scanning path, affecting the recorded signal.

The response of the sensor to the aluminium inserts can be explained by the CPD theory as illustrated in Fig. 15. The surface charge generated due to the CPD between the insert and the steel on the cross-section had a square-shaped distribution as shown in Fig. 15 (a). When the sensor face passed over the aluminium insert which exhibited a negative charge, electrons within the sensor face were repelled, resulting in the generation of an electron flow. The detected charge is shown in Fig. 15 (b). The electron flow was converted into a proportional voltage output by a charge amplifier. The voltage signal was further transformed into a digital output through a data acquisition card. Finally, by applying the amplification ratio, the detected charge was calculated and determined.

The shape of the detected charge signal can be attributed to the circular shape of the aluminium insert and the response of the electronics and filters within the charge amplifier. As the sensor passed over the insert, the overlapped area between the sensing element and the insert varied, increasing as it approached the insert and decreasing as it moved past the insert as seen in Fig. 15 (c). This fluctuation in the overlapped area directly impacted the amount of charge interaction between the sensor and the insert. Consequently, the amplitude of the detected charge exhibited an initial increase followed by a decrease, resulting in a 'bell' shaped response rather than an inverted 'top hat' response. Additionally, the shape of signal can also be influenced by the behaviour of the charge amplifier in the sensing system. The charge amplifier has inherent limitations, such as a restricted bandwidth and prolonged rise time, which means it cannot respond instantaneously to rapid changes in the input signal. Furthermore, the filtering components and parasitic capacitance within the charge amplifier can introduce
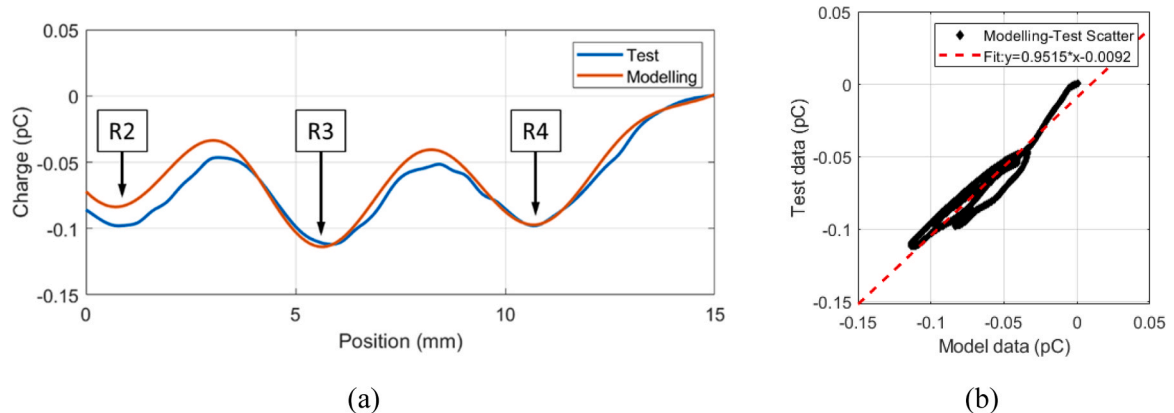
Fig. 14. (a) Test and modelling data for bar sensor response to Al inserts (b) Linear regression models between modelling and experimental data.
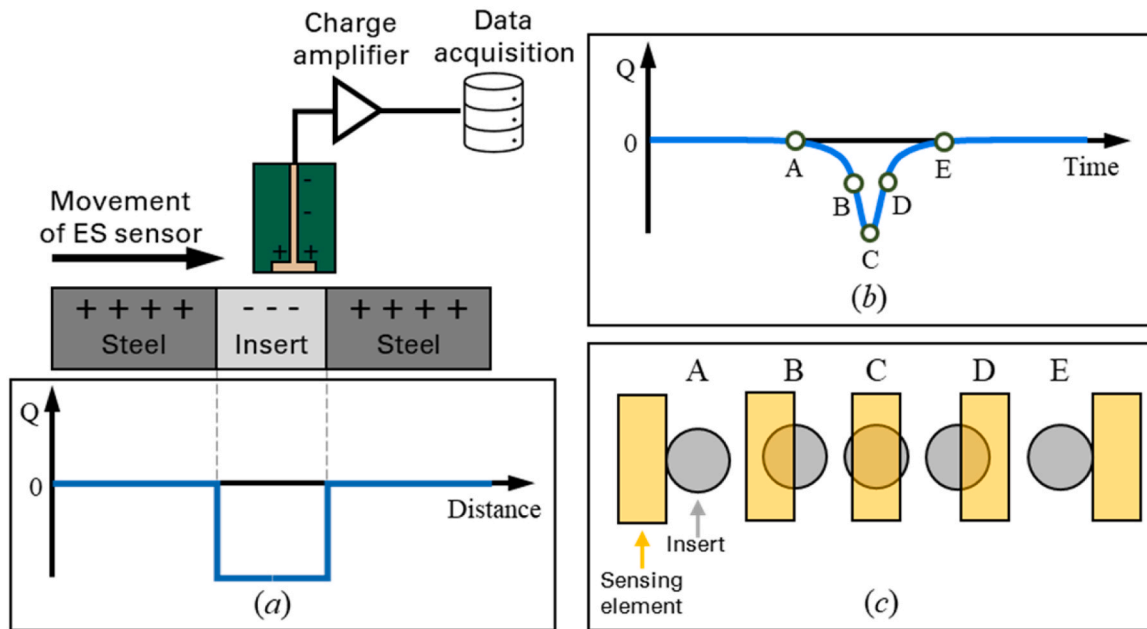
Fig. 15. Schematic diagram explaining the sensor response: (a) Real charge caused by the CPD between steel and insert on the cross-section (b) Signal of the detected charge (c) Changes in overlapped area when the sensor passing the insert.

phase shifts and distortions to the signal.

3.1.2. Array sensor calibration results

The response of array sensor to aluminium inserts with the clearance of 0.4 mm are shown in Fig. 16. In the case of Ch1, the inserts R1, R2, R3 and R4 were captured. Due to the limitation of the sensor's scanning path, only R2, R3 and R4 were detected by Ch 2 and Ch3. The signal for R1 was weaker than the signals for R2 and R3 due to the different number of inserts. R1 contained only one insert, whereas R2 had two inserts and R3 had three inserts and R4 had two inserts. The signal strength being directly to the number of inserts. The signals for the insert rows were observed to be 2 mm away from the signal for the same row detected by adjacent channels, which aligned with the distance between the adjacent sensing elements. This shows that the array sensor exhibited consistent detection of the aluminium inserts, demonstrating good repeatability. The length of the signals generated during the sensing element's passage over the insert rows was measured to be 5 mm, corresponding to the length that the sensing element passing the rows as shown in Fig. 17.

The comparison of the experimental and simulated response of Ch2 to aluminium inserts for four different clearances (0.2, 0.4, 0.6, and 0.8 mm) is presented in Fig. 18. It is worth noting that a strong

correlation between experimental data and modelling data was observed within the initial 12 mm of the scan where the inserts were positioned. However, when the sensor was at 12 mm to 15 mm positions, a relatively weaker correlation was observed. This can be attributed to angular misalignment between the sensor face and the sample, i. e., the sensor and the sample were not perfectly parallel. A slight incline, causes the clearance to decrease near the 15 mm point, which, in turn, resulted in larger signals in this region.

As depicted in Fig. 19, a linear regression analysis was conducted on the experimental and simulated data within the 0–12 mm positions for the four different clearances. The gradient and R-squared values for the four models are listed in Table 5. The gradients of the fitted lines for the four clearances were determined to be 1.265, 1.414, 1.441, and 1.393, respectively. The R-squared values were found to be close to 1, suggesting an acceptable level of agreement between the simulated and experimental data. Notably, the R-squared value exhibited a decline for the smallest (0.2 mm) and largest clearance (0.8 mm). For the clearance under 0.2 mm, the decline was attributed to the inherent error associated with setting up the clearance, which relied on a feeler gauge with a tolerance of 0.05 mm. Consequently, as the clearance diminished, the error percentage magnified, leading to a reduction in the R-squared value. With a large clearance setting (0.8 mm), the increased distance
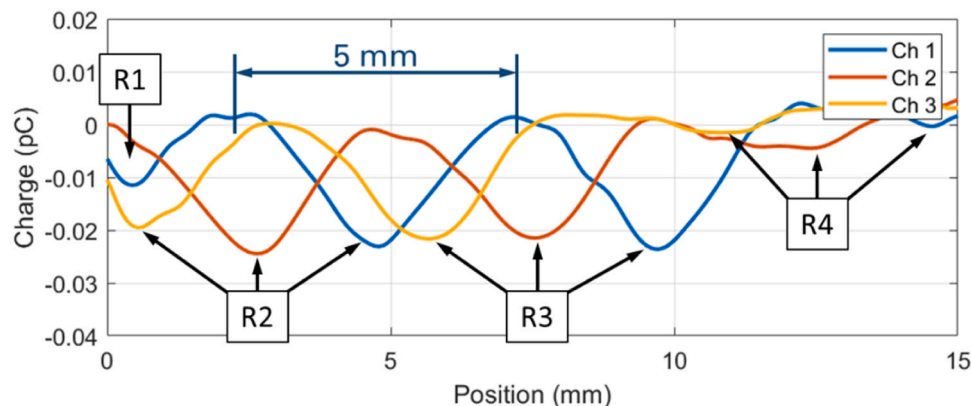
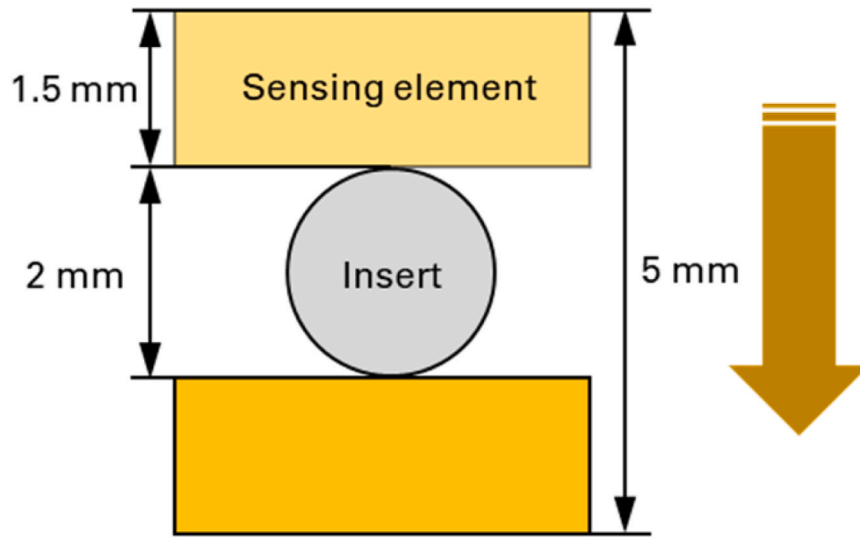**Fig. 16.** Array sensor response to Al inserts.

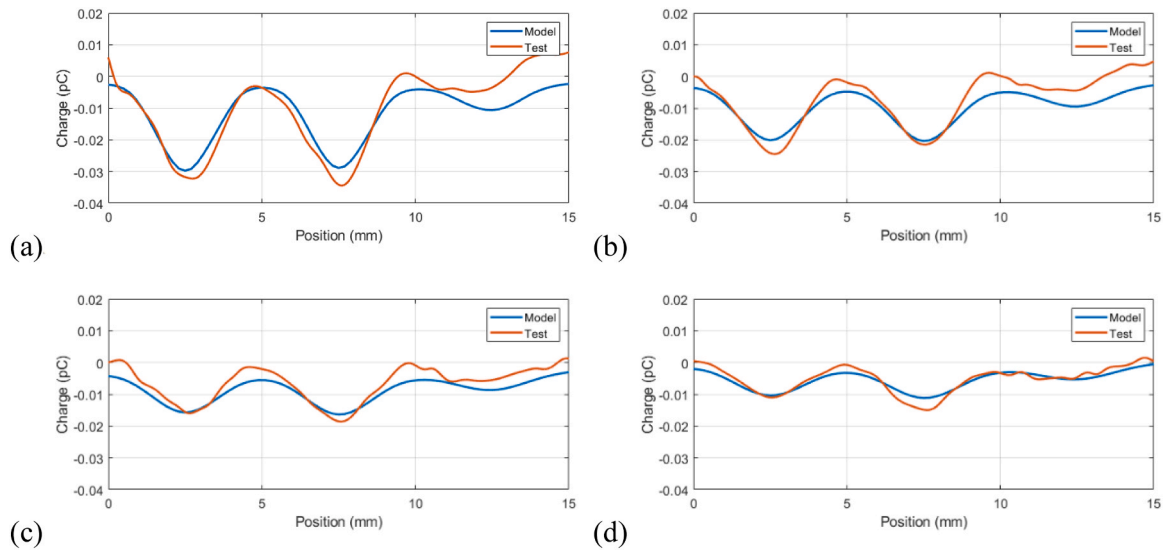**Fig. 17.** Sensing element's passage over the insert.

Fig. 18. Comparison of test and modelling charge data for array sensor response to Al inserts under clearances of (a) 0.2 mm (b) 0.4 mm (c) 0.6 mm (d) 0.8 mm.

between the sensor and the sample could reduce interaction between surface charges and the sensor, affecting the sensitivity of the measurements. Furthermore, variations in clearance may influence environmental conditions such as airflow and humidity, further influencing surface charge behaviour. Therefore, a clearance range of 0.4–0.6 mm is deemed suitable for sensor operation, and a clearance of 0.4 mm was selected for subsequent wear tests.

A comparison of the sensor data for aluminium, solder and steel inserts under 0.4 mm is presented in Fig. 20. It can be observed that the solder inserts generated negative signals, similar to the aluminium inserts, owing to their lower work function in comparison to steel. Furthermore, as anticipated, the signals generated by the solder inserts were lower than those generated by the aluminium inserts. This difference can be attributed to the fact that the work function of solder is higher than that of aluminium. As a result, the CPD between the solder inserts and steel is smaller, leading to reduced signal amplitudes. The steel inserts were composed of the same materials as the plate, ensuring that no differences in work function existed between the inserts and the plate. Consequently, no visible CPD was detected at the presence of the inserts.

3.2. Tribological feasibility test results

3.2.1. Bar sensor test results

Fig. 21 displays (a) the root mean square (RMS) coefficient of friction derived from reciprocating friction loops and the (b) electrostatic data captured by the bar sensor during Test 1 (Section 2.3.2). The root mean square (RMS) of the coefficient of friction, with mitigation of spikes at the stroke ends, was computed across positions ranging from 1.5 mm to 23.5 mm, as illustrated in Fig. 12. The friction shows a gradual increase, reaching a steady state of approximately 0.45 after 600 cycles in this dry wear test. Simultaneously, the electrostatic data reveal charge formation on the wear scar, notably demarcated at a 12.5 mm displacement position at the stroke end. Both friction and electrostatic data exhibit a consistent pattern of initial increase followed by stabilisation, correlating robustly with wear scar development. The concurrent patterns of these data sets imply a direct correlation between the evolution of frictional forces and electrostatic charges.

3.2.2. Array sensor test results

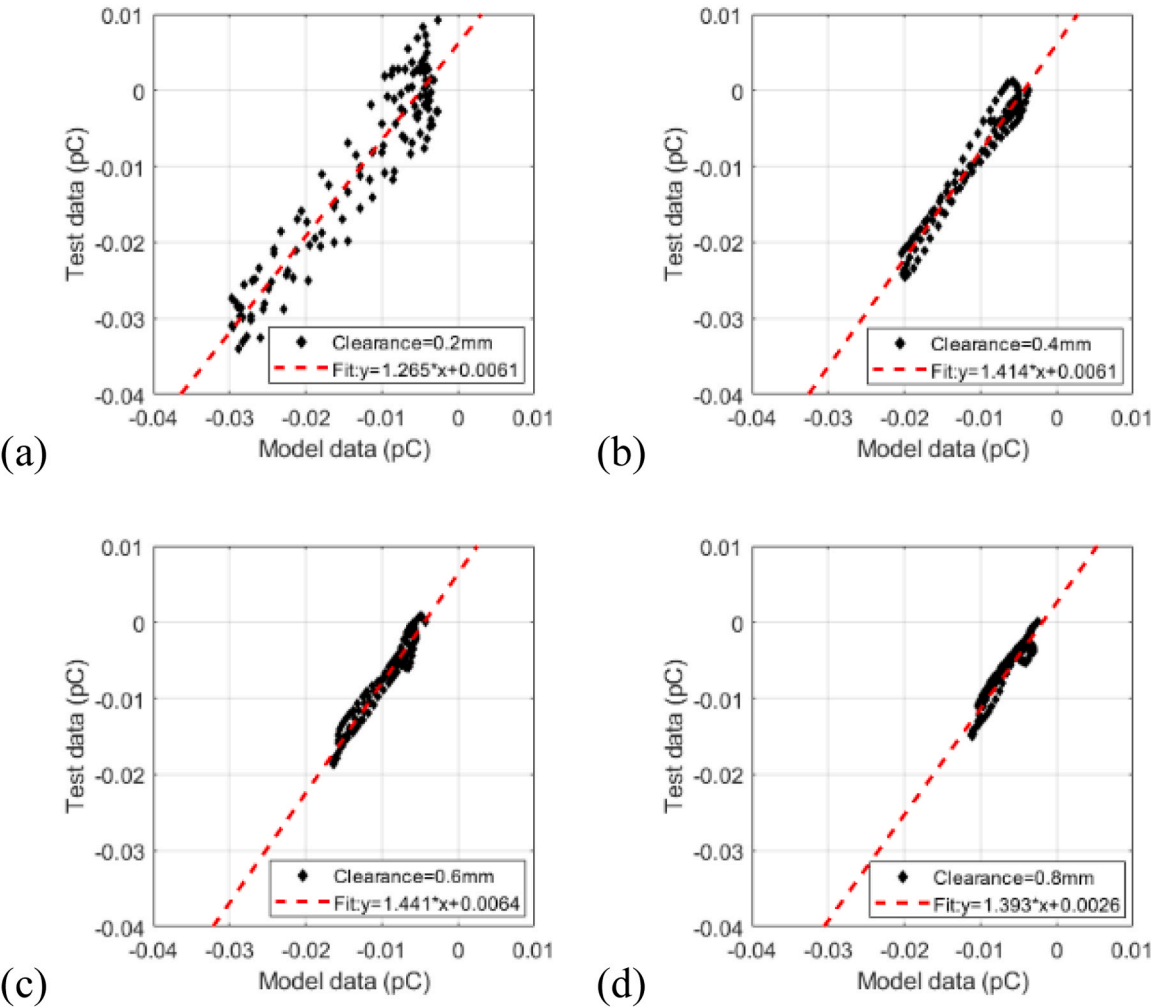The charge maps generated using the array sensor after Test 1 and

Fig. 19. Linear regression models for clearances of (a) 0.2 mm, (b) 0.4 mm, (c) 0.6 mm, and (d) 0.8 mm for 0–12 mm positions.

Table 5
R-squared and gradient values for various clearances acquired from Fig. 19.

Clearance (mm)	0.2	0.4	0.6	0.8
Gradient value	1.265	1.414	1.441	1.393
R-squared value	0.89	0.96	0.96	0.90

Test 2 are shown in Fig. 22. It is evident that the wear scar exhibited positive signals in comparison to the uncontacted materials which agreed with the response of the bar sensor. Furthermore, since more wear was accumulated after Test 2, the signals generated from the wear scar following Test 2 were observed to be more pronounced than those generated from the wear scar after Test 1.
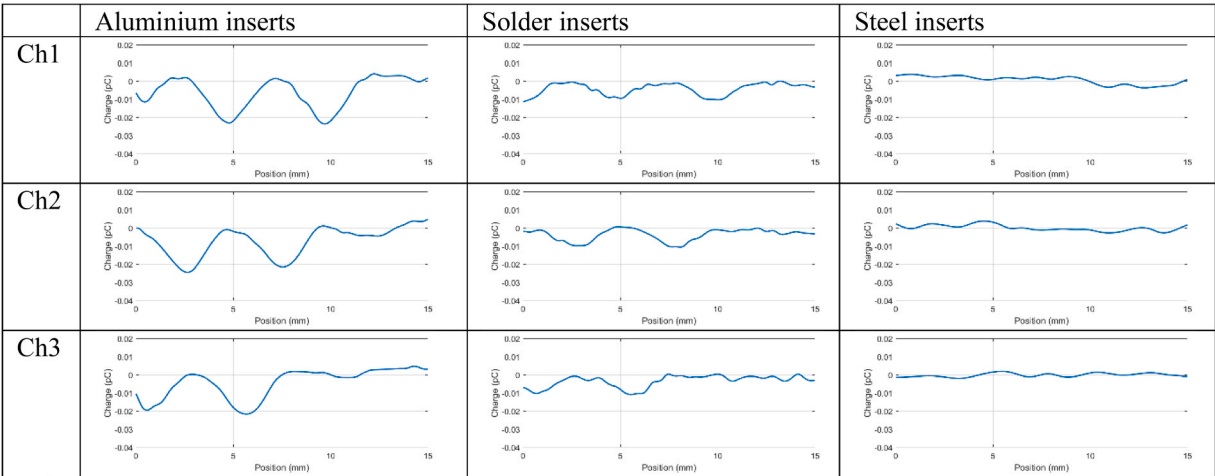

Fig. 20. Comparison of response of the three sensing elements (Ch1, Ch2, Ch3) to Al, solder and steel inserts.
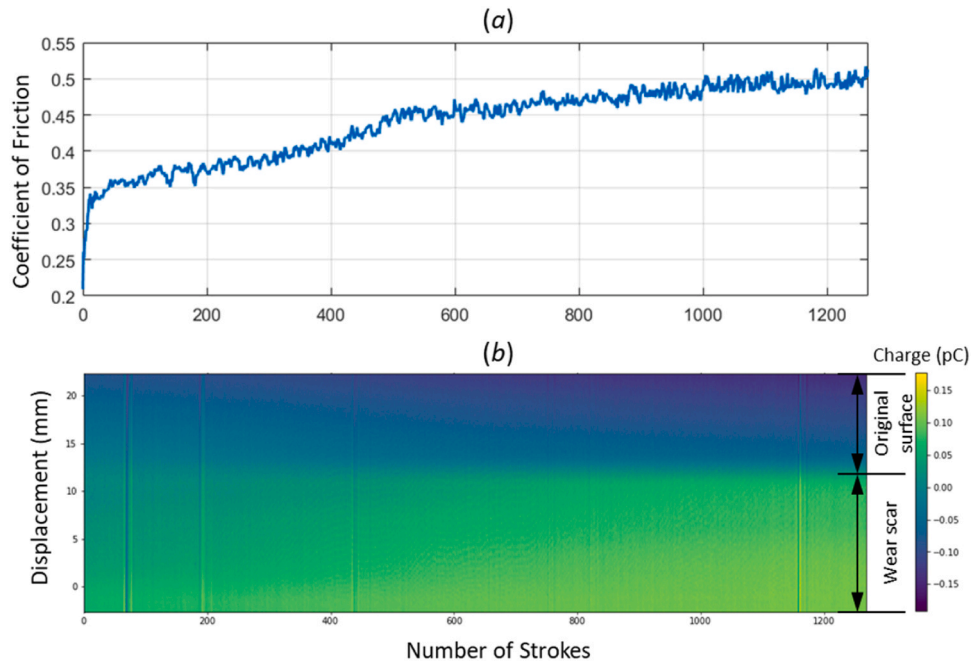
Fig. 21. (a) RMS of Coefficient of Friction during Test 1 (b) ES online signal recorded by bar sensor during Test 1.
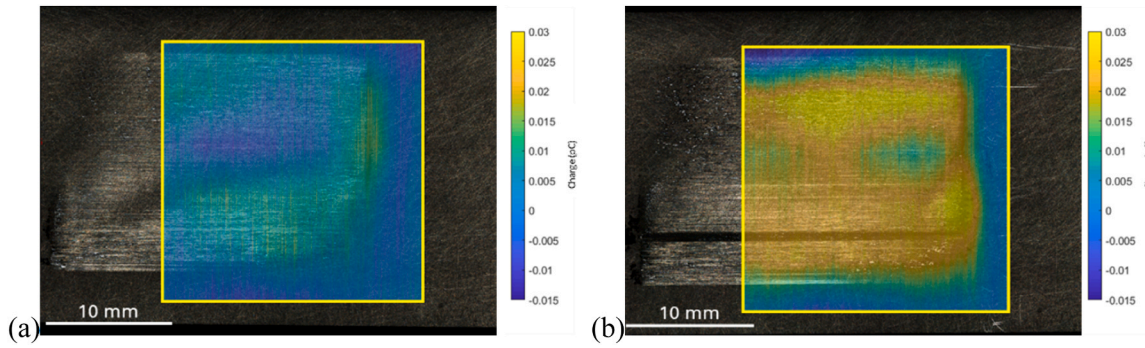

Fig. 22. Charge map generated using array sensor after (a) Test 1 (Load=10 N, reciprocating frequency=1 Hz, stroke length=25 mm, duration=20 minutes) and (b) Test 2 (Load=15 N, reciprocating frequency=1 Hz, stroke length=25 mm, duration=20 minutes).
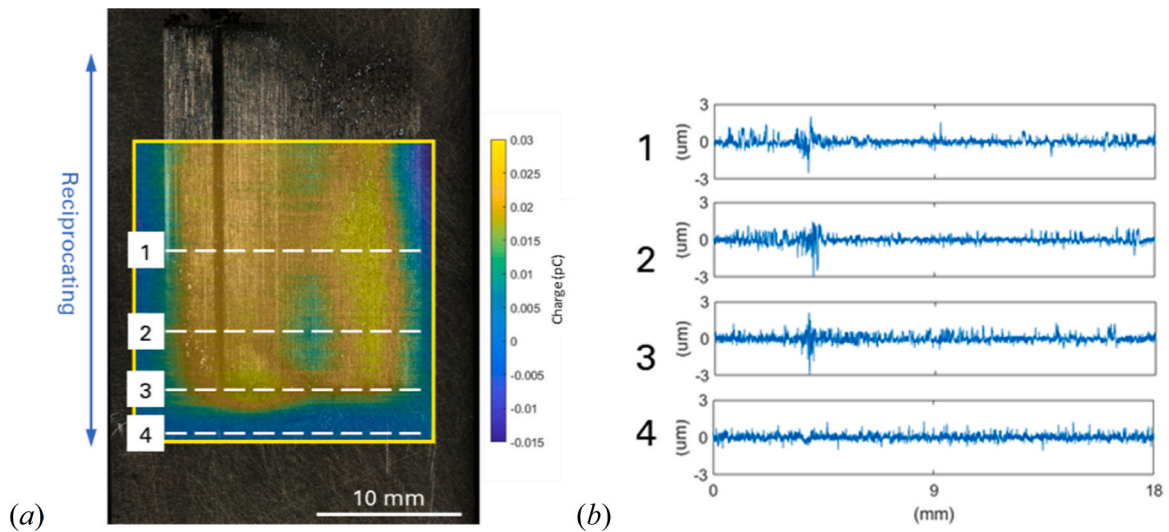

Fig. 23. (a) Charge map for wear scar in Test 2 (b)Surface profiles of the wear scar in Test 2.

After Test 2, surface profile measurements were performed both within and outside the wear scar and the corresponding profiles were presented in Fig. 23. Measurement 1, 2, 3 were within the wear scar while 4 was outside the wear scar. Notably, minimal discrepancies were observed between the surface profiles within the wear scar and those outside of it, except for the presence of grooves at the position of 4 mm. This suggests that the wear was mild and did not significantly modify the surface geometry. Consequently, the generated charge within the wear scar cannot be attributed to variations in the clearance between the plate and the sensor face.

To explain the sensor data, Scanning Electron Microscopy (SEM) and Energy-Dispersive X-ray Spectroscopy (EDS) analyses were conducted on the plate sample after Test 2. The analyses were conducted on three regions displaying different signal strengths, as shown in Fig. 24. The presence of dark dispersed pads distributed across the sample surface shown in the SEM images exhibited high concentrations of oxygen in the corresponding EDS maps, indicating oxidational wear generated in these areas.

The oxide film of steels in air can take the form of three basic iron oxides, FeO, Fe_2O_3, and Fe_3O_4 [29,30] and exhibits a layered structure. The uppermost layer is Fe_2O_3, while beneath this lie layers of Fe_3O_4 and finally FeO next to the metal itself [31]. The Fe_2O_3 top layer is associated with high coefficient of friction of 1.1 and the Fe_3O_4 layer provides a much lower coefficient of friction. In this work, the measured friction coefficient induced by the oxide film was 0.33. Therefore, it is reasonable to conclude that Fe_3O_4 was the predominant oxide on the surface.

Notably, in regions A and C, the weight proportions of oxygen were elevated, reaching as high as 10.3%. Conversely, in region B, the oxygen proportion was comparatively low, at 3.9%. This discrepancy indicates that the accumulation of oxidational wear was more pronounced in regions A and C. Correspondingly, the charge signals observed in regions A and C exhibited higher values, ranging from 0.025 to 0.03 pC, while in region B, the signal ranged from 0.005 to 0.01 pC. This observation suggests that the primary mechanism responsible for the generated charge is associated with the CPD between the oxidised regions and the nascent regions. This verification, that the signal from the electrostatic sensor is linked to the presence of localised oxidational wear, signifies the use of electrostatic charge monitoring as a valuable tool for detecting variation in the severity of surface wear and the inhomogeneity of it.

4. Conclusions

This study investigated the detection of contact potential differences (CPD) induced by dissimilar metals and oxidational surface chemistry using an electrostatic bar sensor and an array sensor. The main findings can be summarised as follows:

- An electrostatic array sensor with enhanced spatial and temporal resolution was developed. This enhanced spatial and temporal resolution was achieved with a smaller sensing area, enabling the detection of localised surface charges and the discernment of complex charge patterns. Furthermore, the sensor's reliability was enhanced by having three sensing elements thereby giving some redundancy. Averaging signals from these three elements effectively eliminated random noise and highlighted signals linked to the features of interest. This noise reduction technique not only enhanced measurement precision but also improved the sensor's effectiveness in accentuating pertinent data.
- Both the electrostatic bar sensor and array sensor were calibrated by known charge patterns induced by a matrix of CPD caused by dissimilar metal inserts. The calibration demonstrated the reliability of the sensors, enabling precise identification of diameters and positions of the metal inserts.
- To validate the performance and reliability of the sensors, COMSOL modelling was employed to simulate the electric fields generated by the metal inserts. The results of these simulations exhibited agreement with the calibration outcomes. This agreement between modelled response and calibration data highlighted the effectiveness of the sensor design and calibration, positioning them as valuable tools for charge pattern detection.
- To identify the surface wear and its variation over the surface, both sensors were employed to detect CPD induced by surface oxidational wear. The bar sensor captured the evolution of oxidational wear and the presence of Fe_3O_4 surface layers. The array sensor captured the charge pattern and presented it in the form of a charge map. This charge map exhibited a notable correlation with the variations observed in localised wear phenomena and patchy oxide film coverage on the surface. Due to the non-uniform distribution of wear across surfaces, relying solely on the bar sensor may overlook vital information about localised wear mechanisms. In contrast, the array sensor demonstrates superior spatial sensitivity compared to the bar sensor, enabling enhanced detection of localised wear phenomena and offering valuable insights into wear distribution. The identification of localised wear patterns holds promise for detecting wear occurrences at earlier stages and monitoring the evolution of wear over time.

Looking ahead and compared with the electrostatic button sensors used previously for gross surface charge measurement, the proposed array sensor will provide greater spatial resolution as using multiple, smaller, sensing faces enables the discrimination of localised surface charge phenomena. Due to the relatively slow change in surface charge distribution with respect to the time taken for the actual sensor
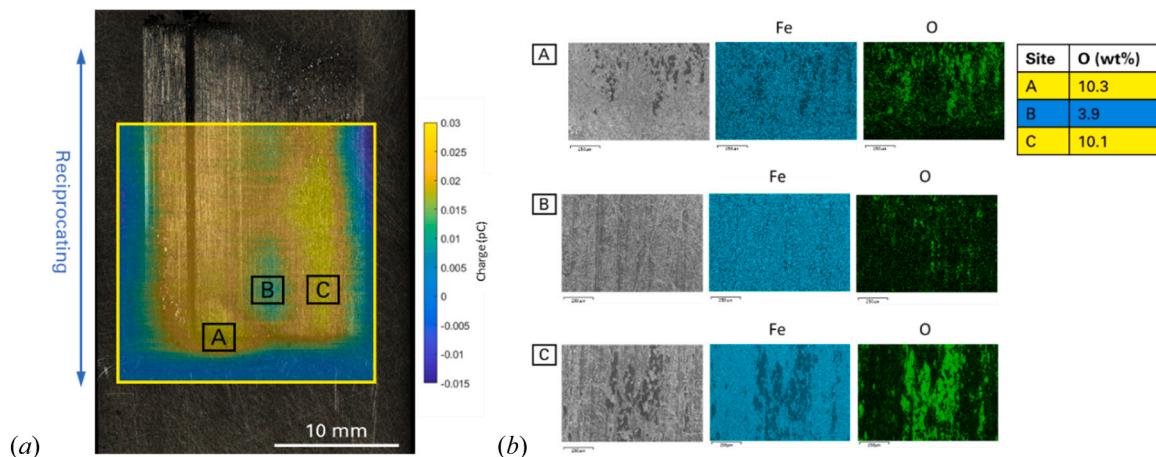

Fig. 24. (a) Charge map for wear scar in Test 2 (b)EDS maps of the wear scar in Test 2.

measurement, a surface charge map may be generated to help highlight the wear distribution and identify associated wear mechanisms. In this instance, it is possible to increase the signal to noise ratio during the evolution of charging events through summing multiple, equivalent signals and averaging them over a suitable period of time.

CRediT authorship contribution statement

Jo Grundy: Methodology, Formal analysis. **Terence Harvey:** Validation, Supervision. **Zaihao Tian:** Data curation. **Ping Lu:** Methodology, Formal analysis, Data curation. **Honor Powrie:** Validation, Methodology, Formal analysis. **Robert Wood:** Supervision.

Declaration of Competing Interest

The authors declare that they have no known competing financial interests or personal relationships that could have appeared to influence the work reported in this paper.

Data availability

Data will be made available on request.

Acknowledgments

References

[1] Y. Yan, et al., Electrostatic sensors–their principles and applications, Measurement 169 (2021) 108506.

[2] Powrie, H., L. Wang, and R. Wood, *Electrostatic monitoring of tribo-contacts: then and now*. WCCM 2017, 2017.

[3] J. Sun, et al., Wear monitoring of bearing steel using electrostatic and acoustic emission techniques, Wear 259 (7-12) (2005) 1482–1489.

[4] J. Booth, et al., The feasibility of using electrostatic monitoring to identify diesel lubricant additives and soot contamination interactions by factorial analysis, Tribol. Int. 39 (12) (2006) 1564–1575.

[5] Morris, S., *Real-time electrostatic charge monitoring of the wear surfaces and debris generated by sliding bearing steel contacts*. 2003, University of Southampton.

[6] T. Harvey, et al., Real-time monitoring of wear debris using electrostatic sensing techniques, Proc. Inst. Mech. Eng. Part J: J. Eng. Tribol. 221 (1) (2007) 27–40.

[7] Powrie, H., et al. *Performance of an electrostatic oil monitoring system during an FZG gear scuffing test*. in Proceedings of the international conference on condition monitoring. 1999. Coxmore Publishing Oxford.

[8] S. Morris, et al., Use of electrostatic charge monitoring for early detection of adhesive wear in oil lubricated contacts, J. Tribol. 124 (2) (2002) 288–296.

[9] Liu, R., et al. *Electrostatic monitoring of wind turbine gearbox under variable operating conditions*. in 2018 Prognostics and System Health Management Conference (PHM-Chongqing). 2018. IEEE.

[10] J. Booth, et al., Scuffing detection of TU3 cam–follower contacts by electrostatic charge condition monitoring, Tribol. Int. 43 (1-2) (2010) 113–128.

[11] S. Morris, et al., Electrostatic charge monitoring of unlubricated sliding wear of a bearing steel, Wear 255 (1-6) (2003) 430–443.

[12] T. Quinn, Review of oxidational wear: Part I: the origins of oxidational wear, Tribol. Int. 16 (5) (1983) 257–271.

[13] S. Lim, The relevance of wear-mechanism maps to mild-oxidational wear, Tribol. Int. 35 (11) (2002) 717–723.

[14] T. Kasai, et al., Applications of a non-contacting Kelvin probe during sliding, Wear 225 (1999) 1186–1204.

[15] Powrie, H., et al. *Electrostatic charge generation associated with machinery component deterioration*. in *Proceedings, IEEE Aerospace Conference*. 2002. IEEE.

[16] B.W. An, et al., Transparent and flexible fingerprint sensor array with multiplexed detection of tactile pressure and skin temperature, Nat. Commun. 9 (1) (2018) 2458.

[17] H. Masuda, et al., Electrification of gas—solid suspensions flowing in steel and insulating-coated pipes, J. Electrost. 2 (4) (1977) 341–350.

[18] D. Armour-Chelu, S. Woodhead, Comparison of the electric charging properties of particulate materials in gas–solids flows in pipelines, J. Electrost. 56 (1) (2002) 87–101.

[19] X. Tang, et al., Analysis of the dynamic sensitivity of hemisphere-shaped electrostatic sensors' circular array for charged particle monitoring, Sensors 16 (9) (2016) 1403.

[20] X. Tang, et al., Compressive sensing-based electrostatic sensor array signal processing and exhausted abnormal debris detecting, Mech. Syst. Signal Process. 105 (2018) 404–426.

[21] J.R. Coombes, Y. Yan, Experimental investigations into the flow characteristics of pneumatically conveyed biomass particles using an electrostatic sensor array, Fuel 151 (2015) 11–20.

[22] J.R. Coombes, Y. Yan, Measurement of velocity and concentration profiles of pneumatically conveyed particles using an electrostatic sensor array, IEEE Trans. Instrum. Meas. 65 (5) (2015) 1139–1148.

[23] X. Qian, et al., Measurement of velocity and concentration profiles of pneumatically conveyed particles in a square-shaped pipe using electrostatic sensor arrays, Powder Technol. 377 (2021) 693–708.

[24] C. Xu, S. Wang, Y. Yan, Spatial selectivity of linear electrostatic sensor arrays for particle velocity measurement, IEEE Trans. Instrum. Meas. 62 (1) (2012) 167–176.

[25] Q. Shi, et al., Simultaneous measurement of electrostatic charge and its effect on particle motions by electrostatic sensors array in gas-solid fluidized beds, Powder Technol. 312 (2017) 29–37.

[26] Y. Yang, et al., Monitoring of particle motions in gas-solid fluidized beds by electrostatic sensors, Powder Technol. 308 (2017) 461–471.

[27] A.M. James, M.P. Lord, Macmillan's chemical and physical data, Macmillan, 1992.

[28] R. Qi, J. Zhang, and, K. Spencer, A review on data-driven condition monitoring of industrial equipment, Algorithms 16 (1) (2022) 9.

[29] T. Childs, The sliding wear mechanisms of metals, mainly steels, Tribology Int. 13 (6) (1980) 285–293.

[30] X. Cui, et al., Research on oxidation wear mechanism of the cast steels, Wear 265 (3-4) (2008) 468–476.

[31] I. Hutchings, P. Shipway, Tribology: friction and wear of engineering materials, Butterworth-heinemann, 2017.

[32] Chen, Su Liang (2009) Development of automated bearing condition monitoring using artificial intelligence techniques. University of Southampton, Engineering Sciences: nCATS Research Group, Doctoral Thesis, 339pp. http://eprints.soton.ac.uk/id/eprint/195557.

Mr. Zaihao Tian received a bachelor's degree in Mechanical Engineering from Xi'an Jiaotong University in 2016, and a master's degree in Mechanical Engineering from Shandong University in 2019. He is currently a Ph.D. student at National Centre for Advanced Tribology at Southampton (nCATS) at University of Southampton. His research focuses on the condition monitoring of surface wear and rolling contact fatigue, and investigation of mechanisms of these failure modes.

Dr. Ping Lu received a B.S. degree from the Beijing Institute of Technology in 2011, and MSc and Ph.D. degrees in Advanced Mechanical Engineering and General Engineering/ Tribology from the University of Southampton in 2012 and 2017, respectively. She is currently serving as an assistant professor at Coventry University and a visiting academic at the University of Southampton. Her research interests include surface engineering, tribological contacts, non-destructive testing, and condition monitoring.

Dr. Jo Grundy received a BSc degree in Chemistry in 1996, and a Ph.D. degree in Organometallic Chemistry in 2003. Then she worked as a Research Fellow in Phosphorous Chemistry at UC Riverside from 2004 to 2005. She joined University of Southampton as a Teaching Fellow in Computer Science in 2018 for one year, and then worked as a Research Fellow for two years. Dr. Grundy currently is a Senior Teaching Fellow. Her research interest is the application of machine learning in sensor data.

Dr. Terence Harvey received a BSc degree in Applied Chemistry in 1994, and a Ph.D. degree in Chemistry in 1997 from University of Portsmouth. He joined University of Southampton in 1997 and now works as a Senior Research Fellow. He has contributed to various projects related to electrostatic sensing, surface engineering, and tribology. His research interests include electrostatic condition monitoring, erosion and erosion-corrosion, and coatings.

Prof. Honor Powrie has worked for General Electric (GE) since 2007 and prior to this held positions with Smiths Aerospace, University spin-out company Stewart Hughes Ltd and RAE Farnborough (QinetiQ). She has nearly 30 years' experience in Machinery Health Monitoring Systems and more than 50 publications on related topics. In her current role as Senior Director of Data Science and Analytics, Prof. Powrie leads GE Aerospace's UK Data Science group, which delivers innovative AI/ML based solutions for managing Aviation assets. Since 2011, she has been a Visiting Professor at University of Southampton. In her role as a Visiting Professor, Prof. Powrie performs industrial liaison activities with the University, including joint research programmes, industrial consultation, PhD project supervision, delivering guest lectures and mentoring.

Prof. Robert Wood is Professor of Surface Engineering and Tribology and has 30 years' experience of tribology and surface engineering. He has spent 4 years at BP before returning to Southampton to re-establish surface engineering/tribology research. His group was awarded £10 M from EPSRC in 2008 to create the National Centre for Advanced Tribology at Southampton (nCATS) and was awarded a further £3 M for research into Green Tribology. He is Chair of UK Tribology and was Editor-in-chief between 2016 and 2021 of the IoP Journal: Surface Topography - metrology and properties. He was elected Fellow of the Royal Academy of Engineering in 2016. He was awarded the Annual Donald

Julius Groen Prize in 2011 and the Tribology Trust Silver medal in 2018 for his outstanding achievements in tribology.